# Evolution of Shell Nonuniformities Near Peak Compression of a Spherical Implosion

## Introduction

In inertial confinement fusion (ICF), a spherical target is imploded by either direct illumination of laser beams (direct drive)[1] or x rays produced in a high-$Z$ enclosure (hohlraum).[2] Target perturbations can result from imperfections in the target itself or from drive nonuniformities. In direct-drive ICF, these include imprinted modulations from laser nonuniformities. These target perturbations can be amplified by hydrodynamic instabilities to disrupt the implosion and degrade target performance. The unstable growth of target perturbations has been extensively studied in planar geometry with preimposed modulations using indirect drive[3,4] and both preimposed and imprinted modulations using direct drive.[5–8] Experiments in cylindrical[9] and spherical[10] geometry have studied effects of convergence on the unstable growth. The modulation growth is typically measured by backlighting the driven target with x rays.[11] The backlighter x rays are attenuated while passing through the target, allowing measurements of the target-areal-density modulations.

Near peak compression in a spherical-target implosion, when the maximum density and temperature occur, the hot, compressed core and inner surface of the shell produce strong x-ray emission. These emissions can be used as a backlighter to probe the outer, colder shell.[12] The first shell-integrity measurements based on this method were time integrated over the duration of peak compression (~200 to 300 ps) of the implosion.[12,13] They used shells with titanium-doped layers and imaging at photon energies above and below the titanium $K$ edge. Core images at photon energies below the $K$ edge (not absorbed by the shell) provide the spatial shape of the backlighter, while core images at photon energies above the $K$ edge (highly absorbed by the shell's titanium) contain information about the structure of shell-areal-density modulations in the titanium-doped layer.

The experiment described in this article, based on the techniques developed in time-integrated experiments,[12,13] is the first measurement of the evolution of shell nonuniformities near peak compression of a spherical-target implosion using targets with titanium-doped layers. The growth of shell modulations in the deceleration phase is measured for the first time in ICF implosion experiments. The core emission, temperature, and shell-areal-density histories are also measured. Areal-density modulations in a titanium-doped layer have been determined from the intensity ratios of time-resolved, two-dimensional (2-D) core images taken above and below the titanium $K$ edge. The average areal density has been measured using streak spectroscopy of titanium absorption of core radiation above the titanium $K$ edge.

## Experimental Configuration

Spherical targets with an initial diameter of about 920 $\mu$m filled with 15 atm of $D_2$ gas were imploded using direct-drive, 351-nm laser illumination on the 60-beam OMEGA laser system.[14] The pulse shape was a 1-ns square with total on-target energy of about 23 kJ. The target shells had 1.9-$\mu$m-thick, titanium-doped (6% by atom) CH inner layers and ~18-$\mu$m-thick, pure-CH outer layers. The initial areal density of titanium in the shell was about 0.05 mg/cm². All laser beams were smoothed with distributed phase plates (DPP's);[15] 1-THz, 2-D smoothing by spectral dispersion (2-D SSD);[16] and polarization smoothing (PS)[17] using birefringent wedges. The average beam-to-beam energy imbalance was about 3.8%. The target emission was imaged on a four-strip framing camera[18,19] by a 6-$\mu$m-diam pinhole array, protected by a 200-$\mu$m-thick beryllium filter. The upper two strips of the framing camera were filtered with a 75-$\mu$m-thick titanium filter, and the lower two strips by a 50-$\mu$m-thick iron filter to image core radiation at photon energies below (~4.8 keV) and above (~6.5 keV) the titanium $K$ edge (4.966 keV), simultaneously.[19] The two x-ray energy channels had spectral bandwidths ($\Delta E/E$) of about 20%. Each image taken with the framing camera had a temporal resolution of ~40 ps and a spatial resolution of about 6 $\mu$m. The framing camera output was captured on a charge-coupled-device (CCD) camera with a 9-$\mu$m pixel size[20] and a magnification of 12.

The spectral evolution of the core emission was captured on an x-ray streak camera[21] with a temporal resolution of ~20 ps.

The streaked spectrum was calibrated by a time-integrated spectrum measured with an ammonium di-hydrogen phosphate (ADP) crystal. Figure 87.16 shows a spectral evolution of core emission as a function of photon energy near peak compression (~2.0 ns) for one of the three similar shots, integrated over the core size for times 1.77, 1.82, 1.92 ns [Fig. 87.16(a)], and 1.97, 2.02, 2.07 ns [Fig. 87.16(b)]. Core images for the same six times on the same shot captured with the framing camera are shown in Fig. 87.17, with the upper six images corresponding to photon energy channel below the titanium $K$ edge, and the lower six images to the channel above the $K$ edge. These images have each been normalized to their highest intensities.

The measured spectra shown in Fig. 87.16 contain information about (1) the evolution of $He_\alpha$, $H_\alpha$, and $He_\beta$ line emission of titanium ions mixed with the core fuel, (2) $1s–2p$ absorption lines (near ~4.6keV) of warm titanium with temperatures

$T$ ~ 500 to 700 eV in the shell, (3) absorption above the $K$ edge (at 4.966 keV) of cold titanium ($T < 500$ eV) in the shell,[12,13] and (4) hot core continuum emission. The effective electron temperature in the emission region $T_e$ and average cold titanium areal density have been calculated by fitting the function

$$I(E) = I_0 e^{\left\{ -E/T_e - \mu_{Ti}(E) \cdot [\rho d]_{Ti} \right\}}$$

to the measured spectra (outside the absorption area of warm titanium near ~4.6 keV, and the shifting $K$ edge), where $E$ is the photon energy, $\mu_{Ti}(E)$ and $[\rho d]_{Ti}$ are the cold titanium mass absorption coefficient and average areal density, respectively, and $I_0$ is the constant. The effect of CH absorption was negligible compared to titanium absorption in these experiments because all time-resolved images below and above the $K$ edge were always identical within experimental noise in shots with CH-only shells (containing no titanium) taken at similar drive conditions.
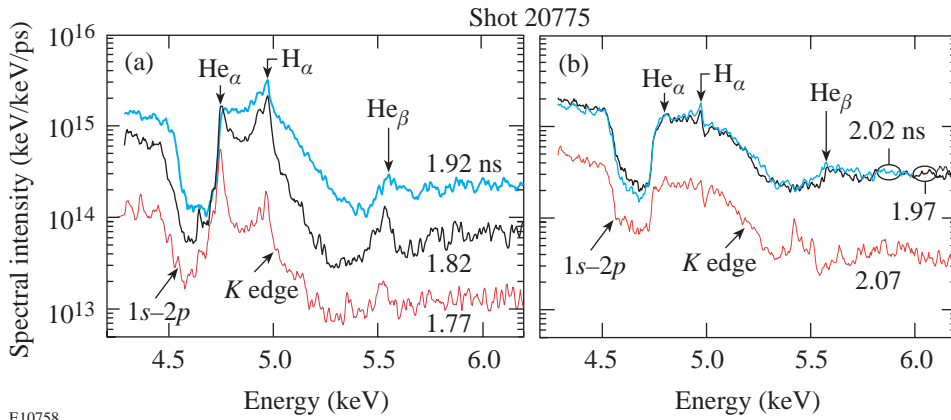


E10758

Figure 87.16
Evolution of core-emission spectral intensity as a function of photon energy for times 1.77, 1.82, 1.92, 1.97, 2.02, and 2.07 ns near peak compression of the spherical implosion.
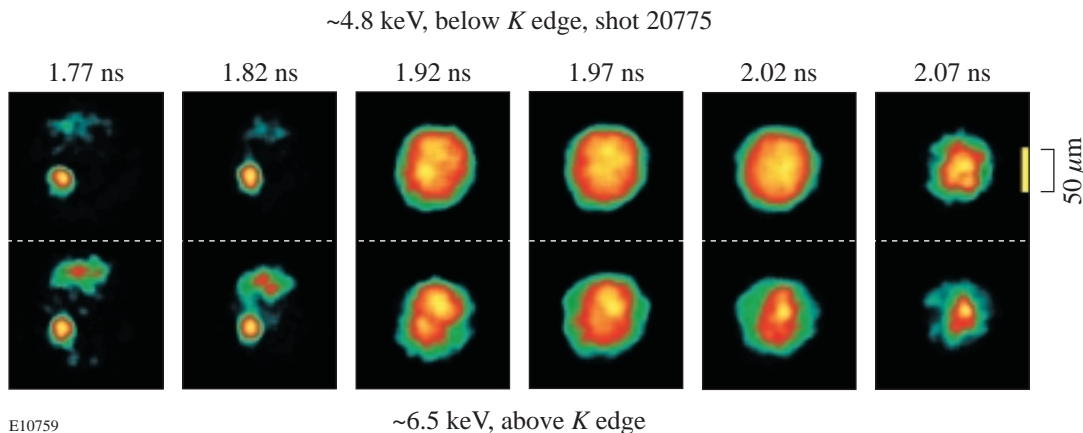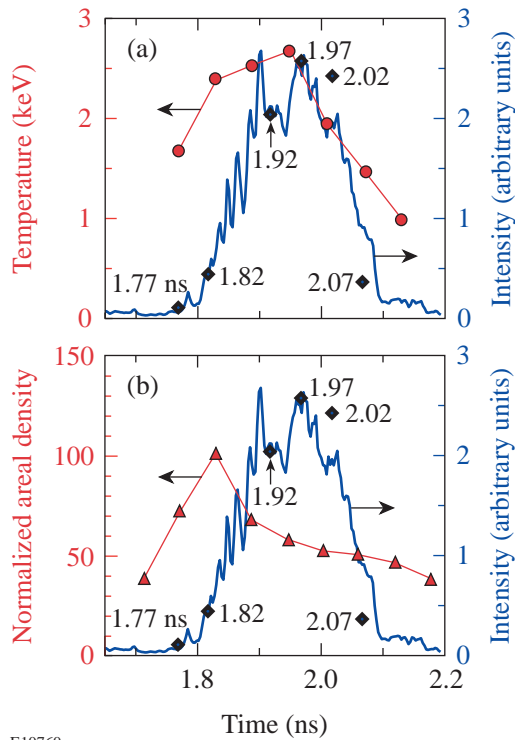
~4.8 keV, below $K$ edge, shot 20775



E10759

~6.5 keV, above $K$ edge

Figure 87.17
"Raw" core images near peak compression at energies below (~4.8 keV, upper row of images) and above (~6.5 keV, lower row of images) the titanium $K$ edge for times 1.77, 1.82, 1.92, 1.97, 2.02, and 2.07 ns.

Figure 87.18 shows a temporal evolution of the electron temperature $T_e$ of the core and the shell-emitting regions [circles connected by a thin solid line in Fig. 87.18(a)] and areal density of the cold titanium in the shell $[\rho d]_{Ti}$ [triangles connected by a thin solid line in Fig. 87.18(b)]. The measured areal density of titanium has been normalized to the initial titanium areal density of the undriven target and represents the amount of compression in the layer. The thick solid lines in Figs. 87.18(a) and 87.18(b) show the evolution of continuum emission intensity in arbitrary units at photon energies of 4.8 to 4.9 keV below the titanium $K$ edge. These were calculated using core emission spectra measured with the streak camera. The diamonds in Figs. 87.18(a) and 87.18(b) show the intensity evolution (in arbitrary units) for the six images (Fig. 87.17) measured with the framing camera, also below the titanium $K$ edge.

The modulations in the cold, or absorbing, part of the shell areal density $\delta[\rho d](\mathbf{r},t)$ at time $t$ ($\mathbf{r}$ is the spatial coordinate) are proportional to the modulation in the logarithm of the ratio of intensities of the two images at photon energies above (highly absorbing by the shell) $I_{>K}(\mathbf{r},t)$ and below (weakly absorbing by the shell) the titanium $K$ edge, $I_{<K}(\mathbf{r},t)$:

$$\delta[\rho d](\mathbf{r}) = \frac{\delta\{\ln[I_{<K}(\mathbf{r})/I_{>K}(\mathbf{r})]\}}{(\mu_{>K} - \mu_{<K})}, \tag{1}$$

where $\mu_{>K} = 0.37\pm0.02$ cm$^2$/mg and $\mu_{<K} = 0.11\pm0.02$ cm$^2$/mg are the spectrally weighed mass absorption coefficients of cold titanium at photon energies above and below the $K$ edge, respectively.[13] The absorption coefficients have been calculated for each time $t$ using the measured x-ray spectra shown in Fig. 87.16 and filter functions of beryllium, titanium, and iron filters.[13] Images $I_{<K}(\mathbf{r},t)$ and $I_{>K}(\mathbf{r},t)$ have been obtained from "raw" images (shown in Fig. 87.17) using the Wiener-filtering technique,[13,19] which was based on the measured system resolution (~6 $\mu$m)[19] and the system noise (determined by the photon statistics of core x rays).[19] All approximations and assumptions made in deriving Eq. (1) have been presented and discussed in detail in Refs. 12, 13, and 19.

**Results and Discussion**

Figure 87.19(a) shows the evolution of areal-density modulations calculated using core images at 1.92, 1.97, 2.02, and 2.07 ns, shown in Fig. 87.17 and Eq. (1), and normalized to their measured (with the streak camera) average areal densities, shown in Fig. 87.18(b). The images at early times 1.77 and 1.82 ns do not have sufficient backlighter area (first two images at ~4.8-keV channel) to probe the nonuniformities in the cold shell. The spatial scale of modulations decreases from time 1.92 ns to time 2.02 ns (as evident from the motion of the red "circular" structure in corresponding images), and then shorter-scale modulations start to grow in the image at 2.07 ns. The image size at 2.07 ns is smaller than images at early times because the level of backlighter emission drops late in the implosion. The effect of titanium line emission on the spatial shape of images below the $K$ edge was negligible because core images, routinely measured with a pinhole-array spectrometer,[12] always had the same spatial shapes at photon energies of titanium (He$_\alpha$, H$_\alpha$) lines and photon energies outside these lines below the $K$ edge. The minimum level of modulations with $\sigma_{rms} = 18\pm8\%$ occurs near 2.0 ns. The modulation $\sigma_{rms}$ decreases by about 20% from time 1.92 ns to time 2.02 ns,



E10760

Figure 87.18

(a) Evolution of core continuum emission temperature (circles), core continuum emission intensity (at 4.8 to 4.9 keV, thick solid line), and emission intensity in images below the $K$ edge (diamonds) for the same times as in Fig. 87.17. (b) Evolution of normalized areal density of titanium (triangles) together with core continuum emission intensity and emission intensity in images below the $K$ edge from (a).

when the maximum core emission intensity and temperature occur (see Fig. 87.18); then it grows by about 60% during decompression while emission intensity and temperature drop.

The shell modulation level at peak compression depends on the initial modulation level at the beginning of the implosion and the amount of unstable growth during implosion. In direct-drive ICF the initial target modulations come primarily from the imprinting[5–8] of laser-beam nonuniformities. Beam-smoothing techniques such as DPP's,[15] SSD,[16] and PS[17] are applied on OMEGA[14] to minimize initial target modulations. To check the sensitivity of shell modulations at peak compression to the initial target modulations, two implosions with similar targets and drive conditions but with different levels of beam smoothing are compared: one shot was taken at best smoothing conditions, including 1-THz, 2-D SSD and PS; the other shot had 3-color-cycle, 0.35-THz, 2-D SSD and no PS. Figure 87.19(b) compares minimum levels of shell modulations near peak compression for these two shots. The level of shell modulation is significantly higher with less-uniform drive using 0.35-THz SSD and no PS ($\sigma_{rms} = 43\pm12\%$) than with 1-THz SSD and PS ($\sigma_{rms} = 18\pm9\%$). Implosions driven with more-uniform beams (1-THz SSD and PS) have primary neutron yields and fuel areal densities ~70% higher than with 0.35-THz SSD and no PS.[22]



**(a)** Shot 20775

1.92 ns    1.97 ns    2.02 ns    2.07 ns

$\sigma_{rms} = 22\%$    18%    18%    29%

$\dfrac{\delta(\rho r)}{\rho r}$  +0.9  0.0  –0.9

**(b)**   1-THz SSD and PS    0.35-THz SSD and no PS

$\sigma_{rms} = 18\%$    $\sigma_{rms} = 43\%$

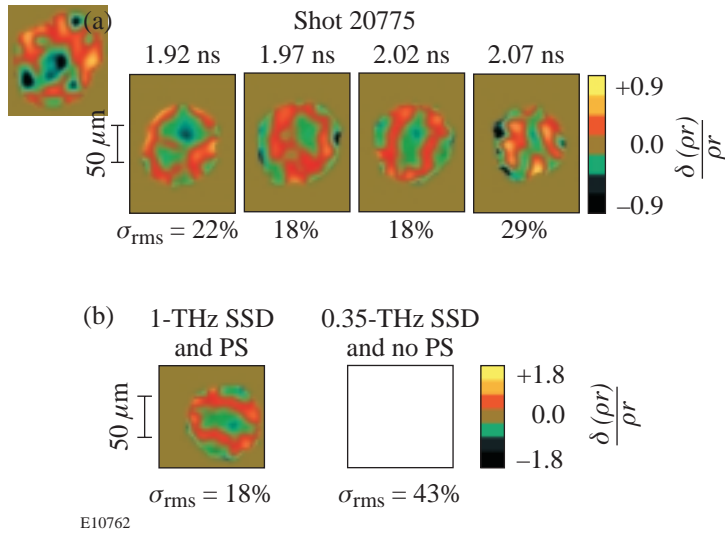$\dfrac{\delta(\rho r)}{\rho r}$  +1.8  0.0  –1.8

E10762

Figure 87.19

(a) Normalized areal-density modulations at 1.92, 1.97, 2.02, and 2.07 ns for shot 20775. (b) Normalized areal-density modulations for two shots: one with 1-THz SSD and PS from (a) at 2.02 ns; the other at peak compression with 3-color-cycle, 0.35-THz SSD and no PS.

A spherical-implosion postprocessor[23] to the one-dimensional (1-D) hydrocode *LILAC*[24] was applied to qualitatively explain the experimental data. This postprocessor uses a sharp-boundary model to study the perturbation evolution in the shell. During the acceleration phase of implosion, when the shell is driven by the laser beams, the shell nonuniformities grow due to the Rayleigh–Taylor (RT) instability.[2–10] When the 1-ns laser drive is turned off, the shell slows down while converging inward to the target center, stops at stagnation, and then moves outward. Since the higher-density shell is slowed down by the lower-density $D_2$ gas, the inner surface of the shell is subject to the RT instability during the deceleration phase. The shell-areal-density modulation (the quantity measured in the experiment) can be written in the following form: $\delta(\rho d) \approx \pi\eta_f + \pi\eta_b$, where $\rho$ is the average shell density, $\eta_f$ and $\eta_b$ are the amplitudes of the front- and back-surface distortions, and $d$ is the shell thickness. During the shell acceleration, when the front surface is RT unstable, the first term $\rho\eta_f$ gives the dominant contribution to $\delta(\rho d)$. In addition, the front-surface perturbations feed through the shell ($\eta_b \sim \eta_f e^{-kd}$, where $k$ is the modulation wave number), seeding the deceleration-phase RT instability on the inner surface. After the laser is turned off and the shell starts to decelerate, the ablation front becomes stable and perturbation $\eta_f$ oscillates. One can estimate the period of such oscillations $T \sim 2\pi\sqrt{R/(\ell g)}$, where $R \approx 60$ $\mu$m is the shell radius, $\ell$ is the mode number, and $g \approx 10^3$ $\mu$m/ns is the deceleration. Substituting results of the 1-D *LILAC*[24] simulation to the above formula gives $T = 600$ ps for the dominant in the experiment mode $\ell = 6$ (which corresponds to a modulation wavelength of about 60 $\mu$m). Therefore, during the time of measurement $\Delta t = 300$ ps, the front-surface modulation changes its sign. Thus, there are two competing effects: first, the reduction of front-surface modulations $\eta_f \sim \eta_0 \cos(2\pi t/T)$ due to phase change, and, second, an increase in back-surface modulations $\eta_b \sim \eta_0 \exp(\gamma t - kd)$ due to the RT growth, where $\gamma$ is the instability growth rate. Initially, $\eta_f > \eta_b$, and the reduction in the front-surface amplitude leads to the reduction in the areal-mass modulation. Later, when $\eta_b$ becomes dominant, growth in shell-areal-density modulation $\delta(\rho d)$ is caused by the exponential growth of the back-surface modulation. An additional reduction in cold $\delta(\rho d)$ could be due to the heating of the inner titanium-doped layer of the shell.

Figure 87.20(a) shows the profiles of target density and temperature in the deceleration phase of the implosion at peak compression (simulated by the 1-D code *LILAC*). The bulk of the shell is dense and relatively cold with an electron temperature less than 1 keV, while the core is hotter and less dense. The

solid line in Fig. 87.20(b) shows the evolution of shell-areal-density modulations calculated with the model for the dominant mode $\ell = 6$ based on the 1-D *LILAC* simulation. The modulations of total shell areal density $\delta(\rho d)$ decrease, while they are dominated by sinusoidally decreasing modulations at the outer surface. When exponentially growing modulations at the inner surface become higher than outer-surface modulations, the total shell-areal-density modulations grow. The circles in Fig. 87.20(b) show that $\sigma_{rms}$ of measured shell-areal-density modulations [shown in Fig. 87.19(a)] follows the model prediction well. The results of the model were normalized to experimental point at $t = 1.97$ ns. The experimental points have been averaged using data from three shots taken at similar conditions. Since the measured spectrum of shell-areal-density modulations is located in the vicinity of the mode
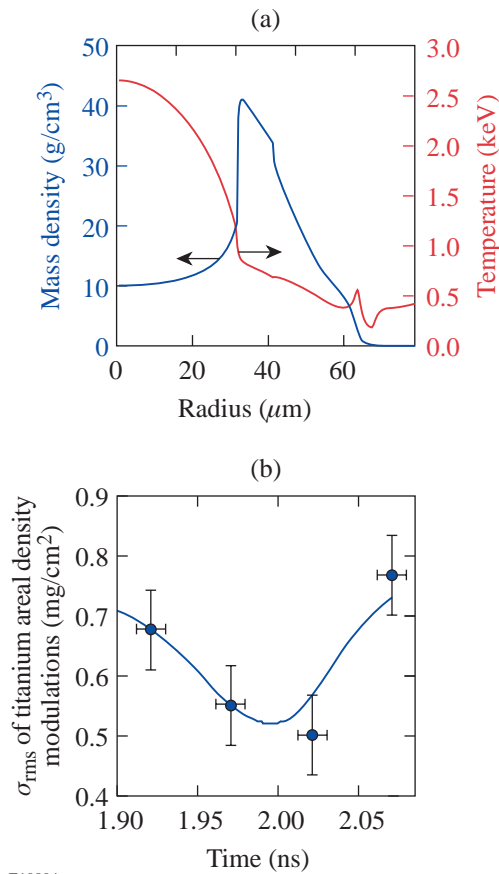
$\ell = 6$ (similar to previous time-integrated measurements[12,13]), the comparison of measured modulation $\sigma_{rms}$ with the calculated amplitude of dominant spectral mode becomes qualitatively reasonable.

Figure 87.18 shows that average cold-shell areal density increases up to ~1.8 ns and then starts to decrease gradually while peak compression is measured to be near 2.0 ns. This indicates that some part of the inner shell mixes with the core fuel and/or heats up to ~2 keV when it stops absorbing core radiation at photon energies above the titanium $K$ edge. Such an increase in shell temperature and the reduction of measured cold-shell areal density are expected in targets with titanium-doped layers because of the additional absorption of core radiation by titanium above the titanium $K$ edge. As a result, the cold-shell average areal density and areal-density modulations may be reduced. This effect may be partially responsible for the decrease of measured areal-density modulations [shown in Fig. 87.20(b)] for times up to ~2.0 ns. The increase of measured areal-density modulation after 2.0 ns, however, should be due to the unstable RT growth in the deceleration phase of the implosion, as predicted by the model.

**Conclusion**

The evolution of shell modulations near peak compression of a spherical implosion has been presented. The minimum level of areal-density modulations, with $\sigma_{rms} = 18\%$, occurs at the peak of core emission with a laser drive that included 1-THz SSD and PS. In implosions using the less-uniform irradiation produced by 3-color-cycle, 0.35-THz SSD and no PS, the level of modulations was significantly higher, with $\sigma_{rms} = 43\%$. The level of measured shell-areal-density modulations decreases when it is dominated by the decreasing modulations at the stable outer surface, then increases when it is dominated by growing modulations at the unstable inner surface, as expected.

Figure 87.20
(a) The simulated profiles of target density and temperature during the deceleration phase of the implosion. (b) The evolution of titanium areal-density modulations in the shell calculated by the model (solid line) and measured (circles).

E10804

REFERENCES

1. J. Nuckolls *et al.*, Nature **239**, 139 (1972).

2. J. D. Lindl, *Inertial Confinement Fusion: The Quest for Ignition and Energy Gain Using Indirect Drive* (Springer-Verlag, New York, 1998), Chap. 6, pp. 61–82.

3. S. G. Glendinning, S. N. Dixit, B. A. Hammel, D. H. Kalantar, M. H. Key, J. D. Kilkenny, J. P. Knauer, D. M. Pennington, B. A. Remington, R. J. Wallace, and S. V. Weber, Phys. Rev. Lett. **78**, 3318 (1997).

4. M. M. Marinak *et al.*, Phys. Rev. Lett. **80**, 4426 (1998).

5. C. J. Pawley *et al.*, Phys. Plasmas **6**, 565 (1999).

6. H. Azechi *et al.*, Phys. Plasmas **4**, 4079 (1997).

7. R. J. Taylor *et al.*, Phys. Rev. Lett. **76**, 1643 (1996).

8. D. H. Kalantar, M. H. Key, L. B. Da Silva, S. G. Glendinning, B. A. Remington, J. E. Rothenberg, F. Weber, S. V. Weber, E. Wolfrum, N. S. Kim, D. Neely, J. Zhang, J. S. Wark, A. Demir, J. Lin, R. Smith, G. J. Tallents, C. L. S. Lewis, A. MacPhee, J. Warwick, and J. P. Knauer, Phys. Plasmas **4**, 1985 (1997).

9. D. L. Tubbs, C. W. Barnes, J. B. Beck, N. M. Hoffman, J. A. Oertel, R. G. Watt, T. Boehly, D. Bradley, P. Jaanimagi, and J. Knauer, Phys. Plasmas **6**, 2095 (1999).

10. S. G. Glendinning *et al.*, Phys. Plasmas **7**, 2033 (2000).

11. S. G. Glendinning *et al.*, in *Applications of Laser Plasma Radiation II*, edited by M. C. Richardson and G. A. Kyrala (SPIE, Bellingham, WA, 1995), Vol. 2523, pp. 29–39.

12. B. Yaakobi, V. A. Smalyuk, J. A. Delettrez, F. J. Marshall, D. D. Meyerhofer, and W. Seka, Phys. Plasmas **7**, 3727 (2000).

13. V. A. Smalyuk, B. Yaakobi, J. A. Delettrez, F. J. Marshall, and D. D. Meyerhofer, Phys. Plasmas **8**, 2872 (2001).

14. T. R. Boehly, D. L. Brown, R. S. Craxton, R. L. Keck, J. P. Knauer, J. H. Kelly, T. J. Kessler, S. A. Kumpan, S. J. Loucks, S. A. Letzring, F. J. Marshall, R. L. McCrory, S. F. B. Morse, W. Seka, J. M. Soures, and C. P. Verdon, Opt. Commun. **133**, 495 (1997).

15. Y. Lin, T. J. Kessler, and G. N. Lawrence, Opt. Lett. **20**, 764 (1995).

16. S. P. Regan, J. A. Marozas, J. H. Kelly, T. R. Boehly, W. R. Donaldson, P. A. Jaanimagi, R. L. Keck, T. J. Kessler, D. D. Meyerhofer, W. Seka, S. Skupsky, and V. A. Smalyuk, J. Opt. Soc. Am. B **17**, 1483 (2000).

17. T. R. Boehly, V. A. Smalyuk, D. D. Meyerhofer, J. P. Knauer, D. K. Bradley, R. S. Craxton, M. J. Guardalben, S. Skupsky, and T. J. Kessler, J. Appl. Phys. **85**, 3444 (1999).

18. C. J. Pawley and A. V. Deniz, Rev. Sci. Instrum. **71**, 1286 (2000).

19. V. A. Smalyuk, T. R. Boehly, L. S. Iwan, T. J. Kessler, J. P. Knauer, F. J. Marshall, D. D. Meyerhofer, C. Stoeckl, B. Yaakobi, and D. K. Bradley, Rev. Sci. Instrum. **72**, 635 (2001).

20. R. E. Turner *et al.*, Rev. Sci. Instrum. **72**, 706 (2001).

21. D. H. Kalantar *et al.*, Rev. Sci. Instrum. **72**, 751 (2001).

22. D. D. Meyerhofer, J. A. Delettrez, R. Epstein, V. Yu. Glebov, V. N. Goncharov, R. L. Keck, R. L. McCrory, P. W. McKenty, F. J. Marshall, P. B. Radha, S. P. Regan, S. Roberts, W. Seka, S. Skupsky, V. A. Smalyuk, C. Sorce, C. Stoeckl, J. M. Soures, R. P. J. Town, B. Yaakobi, J. D. Zuegel, J. Frenje, C. K. Li, R. D. Petrasso, D. G. Hicks, F. H. Séguin, K. Fletcher, S. Padalino, M. R. Freeman, N. Izumi, R. Lerche, T. W. Phillips, and T. C. Sangster, Phys. Plasmas **8**, 2251 (2001).

23. V. N. Goncharov, P. McKenty, S. Skupsky, R. Betti, R. L. McCrory, and C. Cherfils-Clérouin, Phys. Plasmas **7**, 5118 (2000).

24. J. Delettrez and E. B. Goldman, Laboratory for Laser Energetics Report No. 36, University of Rochester (1976).